A new pure ion plasma device with laser induced fluorescence diagnostic

F. Anderegg, X.-P. Huang,[a) E. Sarid,[b) and C. F. Driscoll
Institute for Pure and Applied Physical Sciences and Department of Physics,
University of California at San Diego, La Jolla, California 92093

We describe a new apparatus for magnetic confinement of a pure ion plasma, with laser diagnostics to measure test particle transport across the magnetic field. In addition to the axisymmetric trapping potential, rotating electrostatic wall perturbation is used to counteract the plasma loss processes, giving steady-state ion confinement for weeks. Electronic spin polarization of the ion ground states is used to label the test particles; this spin orientation is controlled by direct optical pumping. The laser-induced fluorescence (LIF) technique is used to nondestructively measure the ion velocity distribution; and an absolute calibration of the charge density is obtained from the LIF measurement of the plasma rotation velocity. Two new technological improvements compatible with ultrahigh vacuum systems have been used: a semirigid Teflon insulated coaxial cable has low microphonic noise, and an antireflective coating is used to reduce reflection of ultraviolet light inside the vacuum chamber. © *1997 American Institute of Physics.* [S0034-6748(97)05206-4]

I. INTRODUCTION

Non-neutral plasmas have exceptional confinement properties and can relax to thermodynamic equilibrium,[1] but little is known about the transport of test particles in a non-neutral plasma. In a Penning–Malmberg trap, the transport due to collisions with neutrals is well understood, and is generally negligible for pressures below 10^{-7} Torr.[2] Anomalous transport, presumably caused by static azimuthal asymmetries in the electric or magnetic field, has been experimentally characterized and extensively documented,[3] but the underlying physics is still unclear. Considerable progress has been made in understanding the ''rotational pumping'' of electron plasmas due to asymmetric end confinement fields.[4] In general, one must first calculate the fields induced in the plasma, and then understand the effect of these fields on particle transport, including the possibility of resonant particles.[5] Measurement of test particle transport can give inside understanding of particle transport in real space and phase space.

In this paper, we report on the construction of an experimental device (called ''IV'') allowing nondestructive measurements of test particle transport in a quiescent, steady-state ion plasma. Spin orientation is a relatively robust way of labeling test particles.[6] Ions have been selected over electrons, because ions have a much larger cross section of interaction with a laser beam. Singly ionized magnesium was chosen for practical reasons, explained later. Optical pumping provides preparation and control of the test particles, while standard laser-induced fluorescence (LIF) techniques are used to perform nondestructive measurements of the ion velocity distribution; an absolute calibration technique of the density has been developed for non-neutral plasmas, and is described later.

Static azimuthal asymmetries and collisions with neutral particles exert a drag on rotating non-neutral plasma, reducing the plasma angular momentum and, consequently, causing radial expansion and losses.[2,3] The new device allows ''unlimited'' confinement of plasmas of up to 10^9 ions: with use of the ''rotating wall'' technique,[7] plasmas are routinely confined for more than two weeks without loss of charge. The technique is based on the idea that angular momentum can be ''injected'' into the plasma by a rotating electrostatic asymmetry on the wall. The plasmas reach a stable equilibrium state, and repeated measurements can be performed on the same plasma.

With various experimental techniques, the ion density, ion temperature, and neutral pressure can all be controlled over a large range of parameters, making this device ideal for the study of test particle transport.

The manuscript is organized in the following way: Sec. II describes the experimental device. Section III is devoted to the diagnostics. The central diagnostic is LIF, and details of its implementation are presented. The optical tagging scheme is also explained. Section IV describes preliminary results obtained with this new device. They are threefold: (a) Absolute density calibration from LIF measurement on a non-neutral plasma. (b) Ion plasmas with very long confinement times have been achieved with the ''rotating wall'' technique. (c) Experimental measurements of test particle transport in non-neutral plasmas are presented.

II. APPARATUS

A. Overview

The overall apparatus is schematically shown in Fig. 1. It consists of an ultrahigh vacuum chamber containing a set of gold-plated cylindrical electrodes immersed in the magnetic field of a superconductive coil. We refer to this geometry as a Penning–Malmberg trap. A pulsed magnesium ion source is used to fill the trap, as we will describe later. The same ions remain confined for weeks by applying a ''rotating wall'' perturbation to one confining electrode. The central diagnostic is nonperturbative and is based on the laser-induced fluorescence technique. For practical reasons ex-

---

[a)Present address: National Institute of Standards and Technology, 325 Broadway, Boulder, CO 80303.
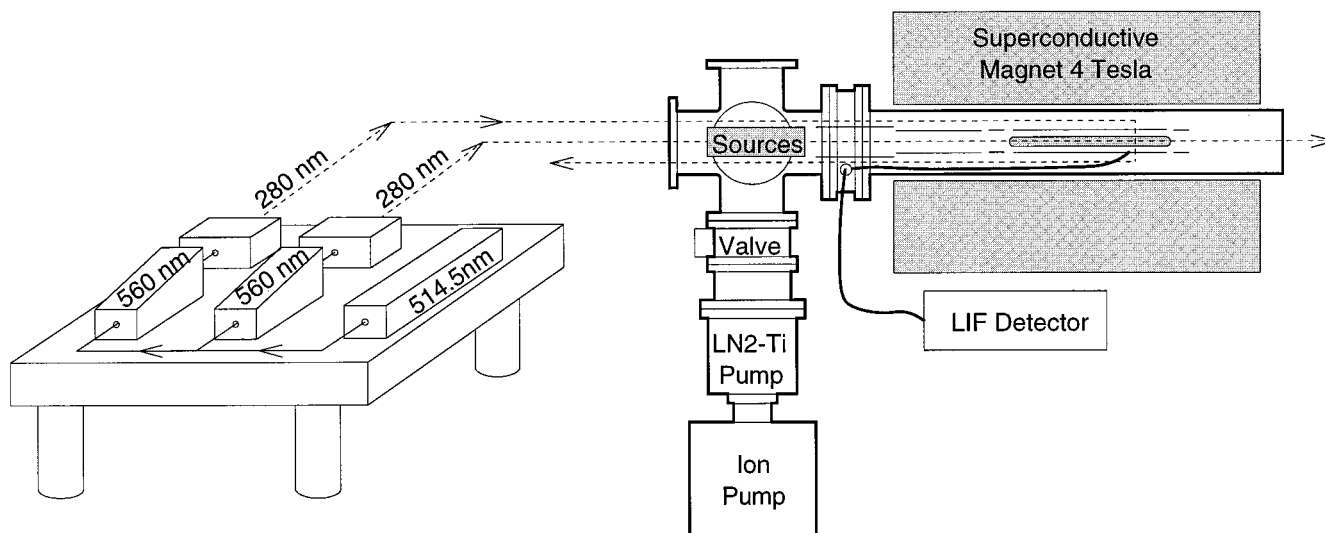[b)Present address: NCRN, P.O. 9001, Beer-Sheva 84190, Israel.

FIG. 1. Schematic overview of the vacuum chamber, superconducting magnet, and laser/detector system.

plained later, the wavelength used is around 280 nm. This ultraviolet (UV) radiation is generated by two cw dye lasers frequency doubled in external cavities.

B. Mechanical engineering

1. Superconducting coil

Pure ion plasmas are, in theory, very similar to pure electron plasmas, and scaling laws have been developed.[8] In order to have ions evolving on orbit similar to electrons, the magnetic field has to be scaled up by the square root of the ion-to-electron mass ratio. Practically, scaling of a prior electron apparatus requires that, for magnesium ions, a uniform axial magnetic field B of about 4 T must be created over the entire confining volume of the trap. In order to achieve steady-state operation over periods of weeks, a superconducting system was chosen. We have a standard niobium titanium copper coil with a 26 cm diam horizontal room-temperature bore. The field uniformity $\Delta B/B$ is less than 0.1% on axis over a length of 30 cm (and less than 1% over 80 cm). Two pairs of orthogonal saddle coils allow precise alignment of the magnetic field with the trap axis.

In order to minimize magnetic-field asymmetries, the entire cryostat has been built out of aluminum. To minimize the liquid helium boil-off, the manufacturer (Cryomagnetics) has installed six retractable current leads for the main coil and saddle coils. For safety reasons in a university environment, all leads are constantly connected to the coils. The standard liquid helium boil-off rate is about 10 ℓ per day with all the current leads installed. The helium gas that boils off the cryostat is recovered and reliquefied by an on-campus facility.

2. Vacuum chamber

Transport due to collision with neutral atoms and molecules is well understood[2] and known to be proportional to the neutral gas pressure. To minimize this transport, most modern non-neutral plasma apparatuses use ultrahigh vacuum (UHV) technology. The vacuum chamber of IV is designed with standard all-metal seal UHV technology. The 25.4 cm vacuum tube (160 cm long), which encloses the electrodes, is made of AISI 310 stainless steel to minimize magnetic-field perturbation. The chamber is equipped with a triode-type ion pump (400 ℓ/s), and a large custom-made titanium sublimation pump (2500 ℓ/s). Initial pumpdown is provided by a dry Venturi pump and three sorption pumps. The background neutral gas pressure in the chamber is measured with two nude ionization gauges and one residual gas analyzer to establish the gas composition.

With all the parts installed in the chamber (electrodes, semirigid cables, nonreflective coating, optical fiber), and after a vacuum bake at 200 °C for one week, the pressure in the system is typically 7×10^{-11} Torr. The main constituents are H_2 (97%) and CO (2.5%).

In order to study the effect of collisions with neutrals on transport processes, the pressure can be increased by closing a pneumatically operated 30.5 cm gate valve, which isolates the pumps from the rest of the apparatus. With the valve closed, outgassing raises the pressure typically to 3×10^{-8} Torr after 4 min. When the gate valve is reopened, pressure falls to below 10^{-10} Torr in less than 10 s.

3. Electrodes and cabling

Longitudinal confinement of ions is provided by positive voltages applied to cylindrical electrodes. Figure 2 describes the electrode arrangement.

A novel technique has been used to accurately position the electrodes. Circular insulator rings have been machined out of Macor (made by Corning Glass) with close tolerances ($\pm 10~\mu$m). They provide centering and tilt alignment of the stack of ring electrodes.

Two of the cylinders (see Fig. 2) are segmented azimuthally, allowing the detection or the excitation of azimuthal charge perturbation modes. One ring has four insulated sectors, positioned 90° from each other and extending 58° each (hereafter, these sectors will be referred to as 90° sectors). A second cylinder is built out of eight insulated sectors, positioned at 45° from each other, extending 27°; these sectors
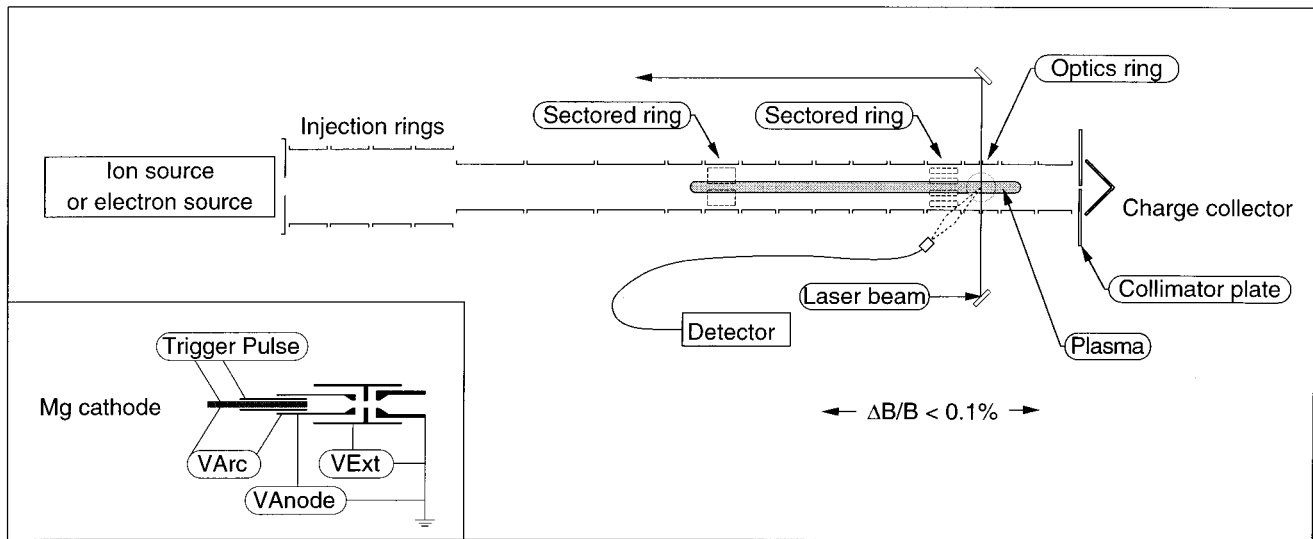
FIG. 2. Electrode arrangement. Each short cylindrical electrode has an inside wall radius of $r_w = 2.86$ cm and a length of $2r_w$. Inset shows the magnesium ion source. The trigger pulse is typically 10 kV. To optimize singly ionized magnesium production, we use $V_{arc} = 50$ V, $V_{anode} = 300$ V, and $V_{ext} = -300$ V.

will be referred to as 45° sectors. Figure 3 shows, on the left, the segmented electrode with eight insulated sectors.

Two other electrodes have special cuts to allow the laser beam to illuminate the plasma and to detect the induced fluorescence. Figure 3 shows, on the right, one of these electrodes. The electrodes are split in half with a 6.35 mm gap to allow a laser beam to scan across the plasma column. The induced fluorescent light is collected through an array of 1 mm diam holes drilled on the sides of the electrode. The size of the holes was kept small enough to avoid perturbing the electrostatic potential of the trap. The overall electrode stack is held together by four compression bars (not shown in Fig. 2).

All electrodes are machined out of oxygen-free high-conductivity (OFHC) copper and plated with a layer of gold (6 μm thick) on a palladium barrier, to prevent the formation of nonconductive oxides when electrodes are exposed to air.

Note that the relatively thick gold plating is required to withstand long exposure (weeks) to elevated temperature during a standard UHV bake; thin plating diffuses more rapidly into the copper, leaving an unplated surface.

The cabling of the inside of the apparatus uses a new type of semirigid 50Ω coaxial cable (manufactured by Precision Tube; type SA 50141). It is made of a central tubular copper conductor plated with silver, surrounded by a splined Teflon insulator, surrounded by copper tubing. The splined insulator allows the cable to withstand 200 °C. This cable was selected for its low noise characteristics in the presence of low-frequency (1 Hz→20 kHz) vibration. In most cables, vibration creates deformations of the dielectric, resulting in charges created by the piezoelectric effect. Another attractive feature of this cable is its low outgassing rate of 8.2 $\times 10^{-7}$ W/m (or 6.2×10^{-6} Torr $\ell/s\ m$ in more conventional units) for an unbaked cable and 1.6×10^{-10} W/m for a cable baked at 200 °C for seven days. All the hardware (screws, nuts, washers, clamps, etc.) used to connect the cabling are made of OFHC copper and beryllium copper to minimize magnetic-field perturbations.

C. Sources

1. Ion source

The magnesium ion source is a metal vapor vacuum arc (MEVVA), similar in its design to the micro-MEVVA developed at Lawrence Berkeley Laboratory.[9] The arc electrode shapes and voltages are shown in the inset of Fig. 2. The ion source is located in the fringing field ($B/90$) of the superconducting coil to minimize the effect of magnetic field on the vacuum arc. The vacuum arc is a pulsed source, and the duration of the arc is determined by the characteristic of the pulse forming network that supplies the arc current. In our experiment, the pulse forming network consists of eight LC stages, each with a 10 μF capacitor and 10 μH inductor, thus, producing a 160 μs flat current pulse. The arc voltage is typically set at $V_{arc} = 50$ V, which results in an arc current of
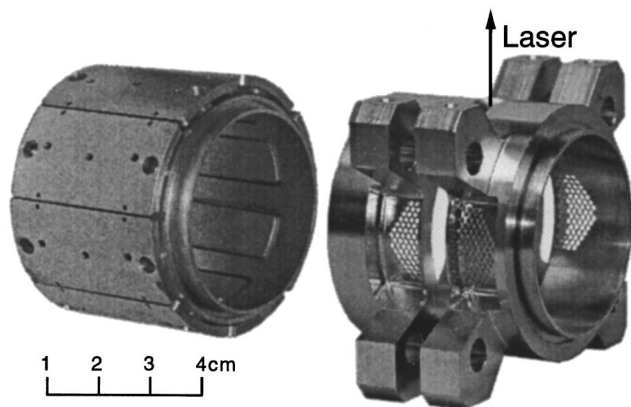

FIG. 3. (Left), azimuthally segmented electrode, with eight insulated sectors positioned 45° from each other. (Right), special electrode for the LIF diagnostic. The laser beam can be sent through the 6.35 mm gap (perpendicular to B) or along the axis of the trap (parallel to B). The LIF detection is orthogonal to the laser beam, and is made through the gap and the array of 1 mm holes drilled on the side.

about 12 A. The ion source is fired, the plasma is trapped as explained in the next paragraph, and then the ion source is turned off. The extractor electrodes ($V_{ext} = -300$ V) extract a neutralized ion beam from the arc plasma.

A pure ion plasma can be trapped in two ways: (a) A large negative potential (typically, -1000 V) is applied to one of the injection rings through which the neutralized ion beam flows. If the beam density is low enough, the negative potential reflects the electrons and lets only ions through; then the ions are trapped in between two cylinders used as gates. (b) An alternative way to produce the confined ion plasma does not require any stripper voltage. The neutralized ion beam is injected directly into the confining region ($V_{conf} \simeq 250$ V). The electrons then escape the confining volume through the ends within one bounce time, while the ions remain trapped.

The magnesium cathode is chemically pure but not isotopically pure, so the resulting Mg plasma has the natural abundance of the stable Mg isotopes: 79% of ^{24}Mg, 10% of ^{25}Mg, and 11% of ^{26}Mg. Both Mg^+ and Mg^{++} are generated; initially, there is typically about three times more Mg^+ than Mg^{++}.[10] Ion cyclotron resonance spectroscopy indicates that after a few hours of confinement with the rotating wall technique, no Mg^{++} can be detected in the trap. This is apparently because Mg^{++} is more chemically reactive than Mg^+; for example, Mg^{++} can transfer one charge to an impurity resulting in Mg^+ and an impurity ion. The chemical reactions with magnesium ions are complex and not yet understood.

Generally, the ion plasma is trapped using the full length of the confining ring in order to trap as much charge as possible. Then the plasma is squeezed to the desired length, by progressively ramping the voltage applied to the individual rings.

The voltage of all the cylinders is arranged to be monotonically increasing with axial distance from the center of the trap, to avoid creating a potential well for electrons. On very long time scales (hours), trapped electrons can ionize the background gas ($P \lesssim 10^{-10}$ Torr) and create unwanted ions, which enter the confining region.

2. Electron source

The apparatus is also equipped with an electron source, in order to more readily allow alignment of the magnetic field to the trap axis. Alignment is obtained to within about 10^{-4} rad by optimizing the number of electrons that remained contained after a given time.[11] Also, the electron source allows us to perform mass scaling experiments.[8] Both ion and electron sources are mounted on a translation table to allow switching and access of laser beams. Electrons are thermally emitted from a spiral-wound thoriated tungsten filament, similar to that of previous apparatuses.[2] The electron filament must also be located outside the main field, in order to heat it with a direct current, yet keep the $\mathbf{j} \times \mathbf{B}$ forces small enough not to distort the spiral. This scheme was chosen for its simplicity over an ac current heating scheme requiring the injection to be synchronized with the ac current in order to achieve the desired filament potential during injection.
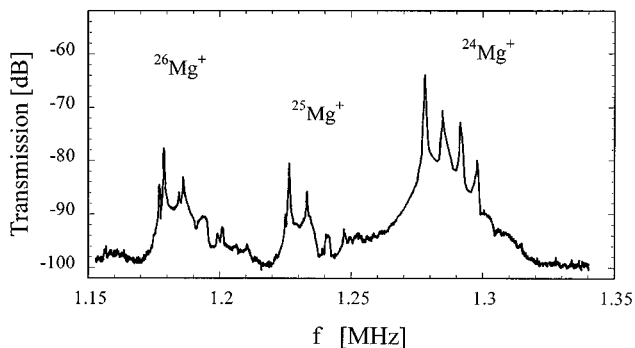

FIG. 4. Ion cyclotron resonance spectrum indicating the existence of magnesium 24, 25, and 26. The ion cyclotron resonances for each species are split into several peaks due to the plasma effects described in Ref. 10.

In order to inject the electron down the magnetic "funnel" (mirror), a series of electrodes referred to as "injection rings" create a longitudinal electric field. The potential of each injection ring is adjusted so as to maximize the electron current reaching the confinement region.

III. DIAGNOSTICS

A. Charge collector

The simplest diagnostic of non-neutral plasmas is a charge collection on a Faraday cup. The measurement is obtained by dumping the plasma through a collimator hole onto the charge collector, by abruptly grounding the end confinement ring. Since the ions stream axially along the B field, a z-integrated density is obtained. By moving the collimator hole and repeating the inject–hold–dump cycle, a radial profile can be obtained. Parallel ion temperature can also be measured by recording the charge collected versus time during a slow dump.[12] These simple destructive diagnostics are not very well suited for ion plasmas, because shot-to-shot fluctuations tend to be large and because the evolution of an ion plasma is slow. However, the Faraday cup charge collector does give an absolute measurement of the charge, which is useful for independently checking the calibration of the laser diagnostic.

B. Ion cyclotron resonant spectroscopy

The ion composition can be qualitatively determined with ion cyclotron resonance spectroscopy (ICRS). Ion cyclotron waves are transmitted from one sectored electrode, and received on the other, separated in z by 37 cm. When the transmitted frequency corresponds to an ion cyclotron resonance for a particular species, the transmission is greatly enhanced, as shown in Fig. 4. In general, the mass of each species can be obtained from this data, but the density of each species cannot be reliably obtained. Detailed measurements of *shifts* in the cyclotron frequencies of each species due to plasma effects have been extensively reported elsewhere;[10] note that in Ref. 10, the base line was set at -80 dB. Once the frequency shifts are understood, ICRS is an accurate and absolute technique to measure unknown masses or to calibrate the magnetic field.

Ion cyclotron resonance can also be used to heat ions of specific charge-to-mass ratio; heated ions will sympathetically heat[13] the other ions of the plasma due to ion–ion collisions. Therefore, an alternative way of performing ICRS is to apply a sinusoidal signal on one sectored electrode and to record the temperature of Mg^+ ions as the applied frequency is slowly scanned. The Mg^+ ions will be heated sympathetically by any species on resonance. Here also, the technique provides an easy identification of the charge-to-mass ratio but the abundance ratio cannot be obtained easily. The temperature measurement of Mg^+ is done with the nonperturbative LIF diagnostic described in the following section.

C. Laser induced fluorescence

1. LIF principles

The ion velocity distribution $f(\mathbf{x},\mathbf{v},t)$ plays a crucial role in almost any plasma process. Laser-induced fluorescence has been used for more than ten years in plasma physics to measure ion velocity distribution both parallel and perpendicular to the externally imposed magnetic field. A review of the diagnostic can be found in Ref. 14. LIF provides *in situ* measurements with negligible perturbations to the plasma and has good spatial resolution, typically, $1-2$ mm^3. Koslover and McWilliams have reported an extension of this technique to measure the complete velocity distribution ($v_\parallel$ and $v_\perp$) referred to as optical tomography.[15]

A single frequency laser beam ($\omega_L,\mathbf{k}_L$) with frequency spread $\Delta\omega_L/2\pi \sim 1$ MHz is used to excite optical transitions in an ion. Ions at velocity $\mathbf{v}$ having an electronic transition frequency ω_0 may be driven to an excited state provided they satisfy the required Doppler shift $\omega_L - \mathbf{k}_L \cdot \mathbf{v} = \omega_0$. The ions in the excited state decay spontaneously and emit a photon flux proportional to the number density of ions satisfying the Doppler-shifted resonance. If the laser is propagating in the $\hat{y}$ direction, scanning the laser frequency yields the one-dimensional ion distribution function $f(\mathbf{x},v_y,t) = \int\int f(\mathbf{x},\mathbf{v},t)dv_x dv_z$. More details on how the signal is collected and processed will be presented below.

2. Ion selection

The criteria for selecting an ion are twofold: Scaling laws[8] from an electron to an ion plasma show that one can design an ion apparatus in which each ion will have the same geometric orbit as the corresponding electron if the magnetic field is scaled by $B_i = B_e\sqrt{m_i/m_e}$. Since one wants to scale an electron apparatus with $B_e = 200$ G, this limits the ion mass to $m_i < 45$ amu due to the prohibitive cost of large superconducting magnets above 6 T. The LIF optical diagnostic requires that the ion has optical transition from the ground state, which can be excited with a laser, either near IR, visible, or near UV. Since we are interested in transport processes that may require hundreds of seconds, no metastable state should exist between the ground state and the excited state, so that the fluorescent signal will not be quenched by optical pumping into the metastable state. The ion should have a spin allowing the use of the spin state tagging method.[6] The ideal candidate should not have hyperfine structure and should be available as a pure isotope. Unfortu-
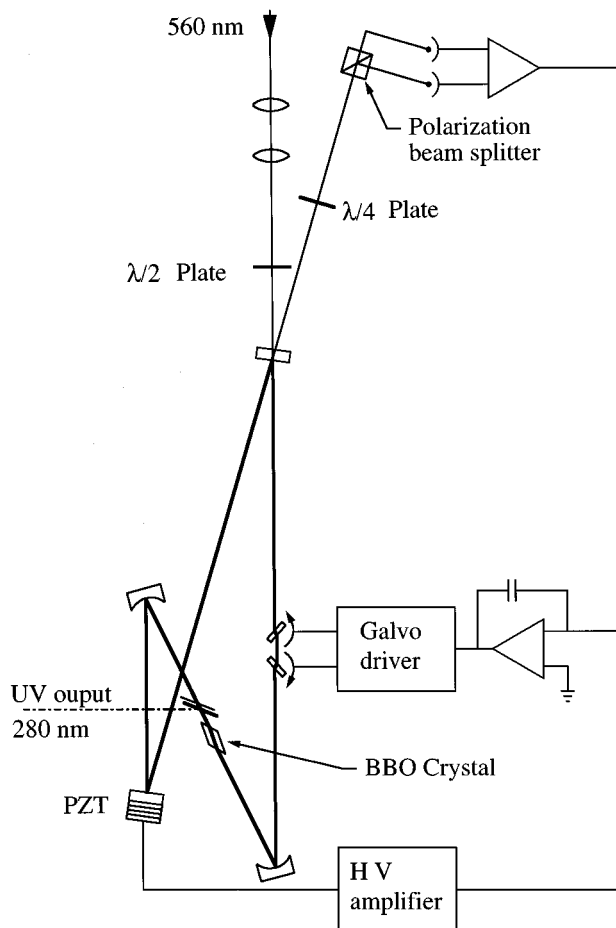

FIG. 5. Frequency doubling cavity to generate cw radiation at 280 nm with a bandwidth of $\Delta\nu_L \simeq 1$ MHz. The polarization sensitive feedback loop is separated into a high-frequency part displacing a mirror mounted on a piezoelectric crystal (PZT), and a low-frequency part driving galvo plates.

nately, nature does not provide the ideal candidate; but singly ionized magnesium ions are fully adequate.

3. cw UV generation

A continuous (cw) laser was chosen based on signal-to-noise considerations and for optimum velocity resolution. Wavelengths of the transition from the ground state $3s^2S_{1/2}$ to the lowest excited states ($3p^2P_{1/2}$ or $3p^2P_{3/2}$) of a Mg^+ ion are in the 280 nm range. Such wavelengths are obtained by frequency doubling of a cw ring dye laser. We use a Bergquist scheme[16] schematically represented in Fig. 5: A nonlinear crystal (beta barium metaborate ''BBO,'' 3 mm×3 mm×5 mm) in an externally stabilized cavity converts the tunable fundamental beam (560 nm, $\simeq 0.7$ W) into an ultraviolet beam (280 nm, $\simeq 15$ mW) with a bandwidth of 1 MHz. The ring doubling cavity is stabilized by a feedback loop using an error signal created by a polarized sensitive detector. The cavity remains locked even as the dye laser is scanned in frequency, and scanning widths of 60 GHz at 280 nm are routinely obtained. This technique has the advantage of not requiring any amplitude modulation.

Figure 6 represents the UV power in the frequency-doubled beam as a function of the power circulating in the
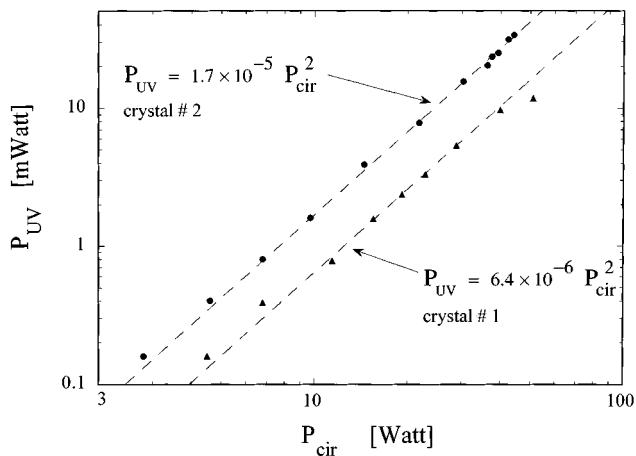
FIG. 6. Efficiency of the frequency doubling. P_{cir} is the power circulating in the cavity at 560 nm and P_{UV} is the UV power at 280 nm extracted by a dichroic beam splitter.

doubling cavity. The ring cavity provides a power enhancement of the fundamental by a factor of 60 with the crystal in the cavity. Note that if the crystal is replaced by a high quality fused silica plate, power enhancement factors up to 120 have been observed. As expected, the UV power is proportional to the square of the fundamental circulating power. Large differences are observed from one crystal to another. Crystal No. 2, which performed best, was manufactured by Cleveland Crystal.

4. Beam transport

The UV laser beam is steered to the apparatus by a series of flat high reflectivity dielectric mirrors. Also, the elliptical aspect ratio of the beam cross section is reduced from about 8:1 to 2:1 by a cylindrical lens. Three of the mirrors are mounted on precision translation tables driven by stepper motors. One mirror provides a selection of beam paths: along the magnetic field to measure the parallel ion velocity distribution function $f(v_{\parallel})$; or perpendicular to the magnetic field to measure $f(v_{\perp})$. The other translation tables scan the beam horizontally across the plasma column, providing $f(x, v_{\perp})$ or $f(x, v_{\parallel})$.

A spatial filter provides adjustable beam size through the plasma column, allowing us to vary the power density. To minimize the unwanted stray light from the beam and to facilitate the alignment, the beam is steered out of the vacuum chamber and its position is monitored on a fluorescent screen.

5. Signal detection

a. Black coating. For our experimental parameters, the LIF light is weaker than the laser beam by about six orders of magnitude. The fluorescence wavelength is almost identical to the laser beam, so great care must be taken to avoid unwanted reflection of the laser beam into the detection system. In the vacuum chamber, multiple baffles are arranged in the beam path and all surfaces are coated with a carbon coating similar to the one applied on the inside of a color cathode-ray tube (Electrodag 181, manufactured by Acheson

Colloids Co.). After proper application (dry nitrogen spray and vacuum bake at 400 °C of all coated parts), the coating is compatible with UHV. Note that if the coating is exposed to air, a 200 °C bake is required to reoutgas the coating. The coating bonds well to OFHC copper and beryllium copper substrates. The outgassing rate after a 200 °C bake is $q_{baked} \leq 4 \times 10^{-9}$ W/m².

b. Telescope. Laser-induced fluorescence light emitted by the plasma is collected by a f2.9 ''telescope,'' shown in Fig. 7. The diagnosed volume is focused onto a 3 mm optical fiber bundle consisting of 94 multimode 280 μm diam fused silica fibers; the orientation of the fibers in the bundle is random. The optical bundle is protected with an aluminum jacket and the entire assembly, as custom made by Fiberguide Industries, is compatible with UHV. The fiber bundle transmits the light to an antireflective-coated fused silica window located at the extremity of a stainless-steel UHV bellows, where the magnetic field from the superconducting coil has decreased to about 400 G. The end of the optical fiber bundle is imaged onto a photon counting photomultiplier tube (PMT) (Thorn EMI 9893QB/350). The tube is shielded from the 400 G magnetic field by two concentric silicon steel pipes and two concentric cylinders of high permeability alloy. Signal pulses from the PMT are amplified with two fast preamplifiers. Finally, pulse height discrimination and counting are performed by a gated photon counter (Standford Research System SR400).

6. Data collection

During each LIF measurement, the laser frequency is scanned 60 GHz across the Doppler-broadened resonance corresponding to the $(3s^2 S_{1/2}, m_j = -1/2 \rightarrow 3p^2 P_{3/2}, m_j = -3/2)$ transition. This ''cycling'' transition does not diminish, since the excited state can only decay back to the original ground state. It is worth noting that under the typical conditions ($B = 4$ T and $T < 4$ eV), the Zeeman levels are completely separated from each other. The scan takes about 1.7 s to complete, during which time the ions bounce axially and $\mathbf{E} \times \mathbf{B}$ drift rotate azimuthally, so the measurement is averaged over z and θ. The intensity of the detected fluorescence during the scan is recorded in the memory of the photon counter in 141 bins, each 10 ms long, with 2 ms dwell time between each bin. The corresponding laser power for each frequency is also recorded with a transient digitizer. Both data sets are then read and saved with a VAX workstation.

We assume that the transition is far from being saturated, so we normalize the received fluorescence intensity by the laser power to compensate for power fluctuations during the scan. We have verified that this assumption is valid for laser power less than 1 mW, as discussed in the subsequent paragraphs. Figure 8 shows the normalized photon count rate as a function of the laser frequency in a typical LIF scan. The solid curve is a six parameter fit to the three-isotope Maxwellian distribution
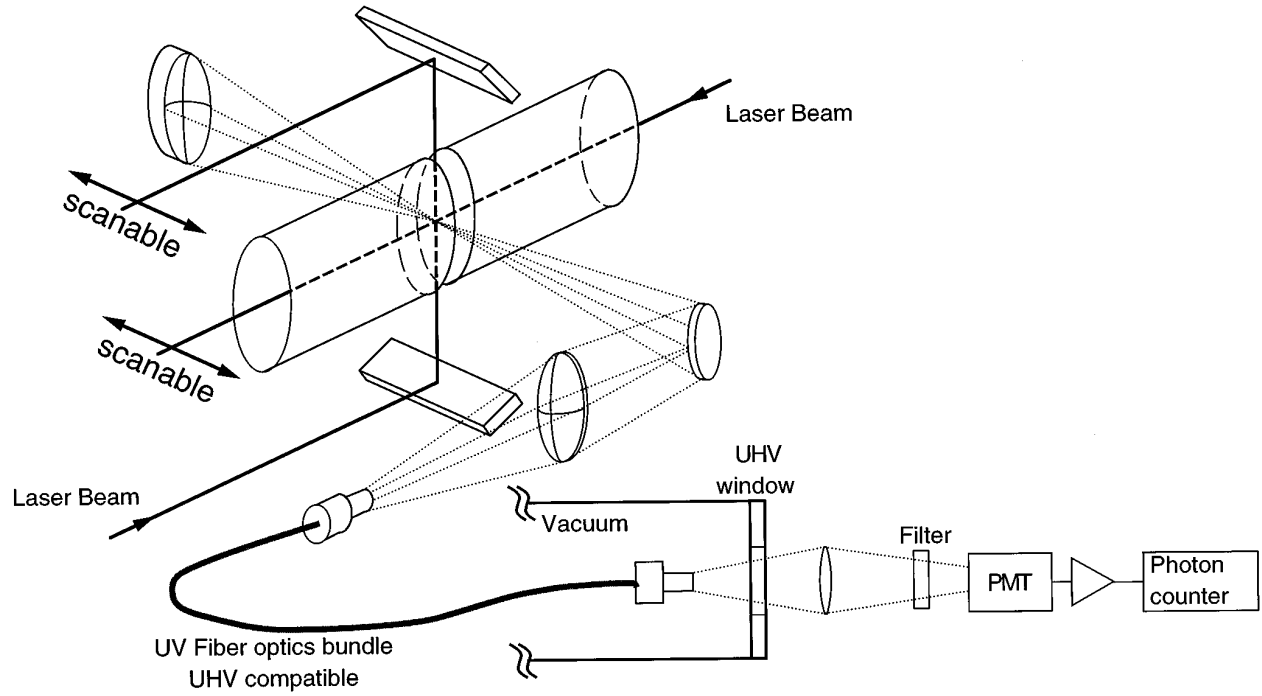
FIG. 7. Schematic of the detection system used to collect the induced fluorescence. Two circular mirrors, one lens, and a fiber optics bundle are installed inside the vacuum chamber. The detector is a photomultiplier tube (PMT) followed by photon counting electronics.

$$N_{\text{photon}} = A_{24} \exp\left\{ -\left[\frac{(f-f_0)}{\Delta f} \right]^2 \right\}$$

$$+ A_{25} \exp\left\{ -\frac{25}{24} \left[\frac{(f-f_0-f_{24/25})}{\Delta f} \right]^2 \right\}$$

$$+ A_{26} \exp\left\{ -\frac{26}{24} \left[\frac{(f-f_0-f_{24/26})}{\Delta f} \right]^2 \right\} + A_0,$$

where A_{24}, A_{25}, A_{26}, and A_0 are proportional to the densities of the $^{24}\text{Mg}^+$, $^{25}\text{Mg}^+$, $^{26}\text{Mg}^+$, and background scattering, respectively, and f_0 and Δf correspond to the total fluid velocity v_y^{total} (see Sec. IV for details) and thermal velocity spread. Here, we assume that the temperatures of the three isotopes are the same locally. The isotope frequency shifts of
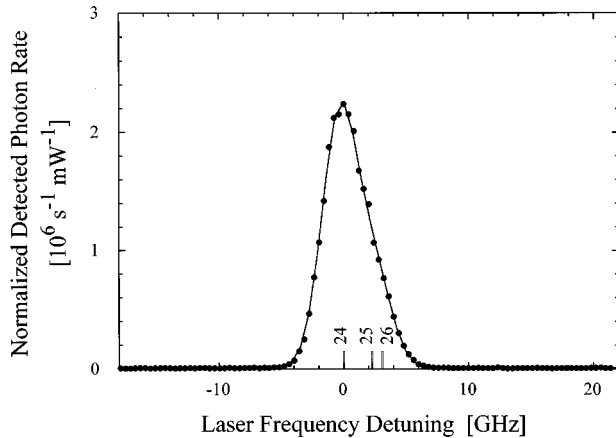

FIG. 8. Detected photon rate normalized by laser power vs laser frequency. The fit to the three isotopes distribution gives $n = 2.73 \times 10^7$ cm^{-3} and $T_i = 0.0375$ eV. The resonant frequency of the three isotopes is shown.

the optical transition are $f_{24/25} = 2.28$ GHz and $f_{24/26} = 3.08$ GHz.[17] It is worth noting that $^{25}\text{Mg}^+$ has a nonzero nuclear spin $I = 5/2$, resulting in hyperfine energy structures. Due to optical pumping effects, a laser beam near the cycling transition frequency will pump most of the $^{25}\text{Mg}^+$ ions to the $(I = 5/2, m_I = -5/2)$ state, causing the disappearance of other spectral lines.[17] The transition we used in the above calculation corresponds to $(S_{1/2}, m_j = -1/2, m_I = -5/2)$ to $(P_{3/2}, m_j = -3/2, m_I = -5/2)$ for $^{25}\text{Mg}^+$.

For temperatures above 0.1 eV, ions with different masses are well mixed radially in the plasma column, and the deviation from a single Maxwellian distribution is not prominent. Below 0.05 eV, the three isotopes cause a visibly non-Maxwellian scan, as seen in Fig. 8. In both cases, the fit to the 141 point data set is very good, indicating that the plasma is well thermalized and that the weak laser beam does not perturb the ions significantly. The relative abundances for each isotope were free parameters of the fit shown in Fig. 8; the results are $^{24}\text{Mg}^+$: 72%, $^{25}\text{Mg}^+$: 13%, $^{26}\text{Mg}^+$: 15%. Note that the natural abundance is $^{24}\text{Mg}^+$: 79%, $^{25}\text{Mg}^+$: 10%, $^{26}\text{Mg}^+$: 11%. The laser frequency was scanned from ''red to blue'' (increasing frequency). The distortion toward heavy isotopes is probably due to the weak effect of laser cooling of $^{24}\text{Mg}^+$ by the beam when it is tuned to the ''red'' side of the transition and heating of $^{24}\text{Mg}^+$ when on the ''blue'' side of the transition. For temperatures above 0.01 eV, where there is negligible isotope separation, we normally assume the natural isotope abundance in the fit, reducing it to four free parameters. With a strong second laser beam, we can cool the plasma below 1 K,[18] where the distribution function is no longer a Maxwellian and must be fitted to a Voigt profile taking into account the finite linewidth of the
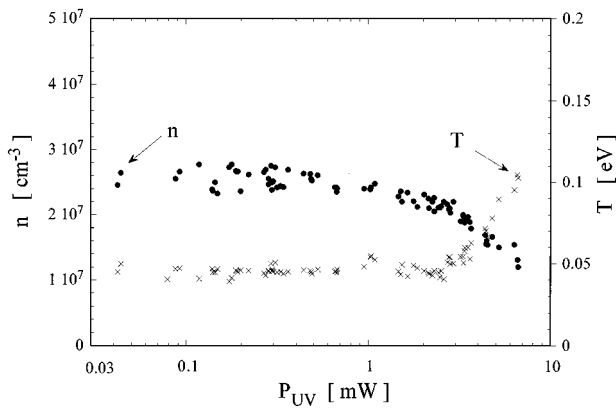
FIG. 9. Measured ion density and temperature vs laser power, showing validity of the linearity assumption below 1 mW, and saturation of the transition above 2 mW.

transition.[18,19] When a large oscillating confinement voltage is applied to modulate the plasma length and produce substantial heating ($T > 3$ eV), the parallel distribution function exhibits a plateau region, typical of a wave damping process.

Radial profiles of plasma density and temperature are obtained by stepping the radial position of the probe beam after each frequency scan. A complete radial profile of about 30 points takes about 1 min to obtain; this includes data acquisition and reading times.

We verify the validity of the linearity assumption by varying probe laser power from 40 μW to 6 mW on the same plasma, and plotting the fitted density and temperature in Fig. 9. For laser power less than 1 mW, the measured density and temperature are independent of power, indicating that the normalization is justified. Above 2 mW, the fitted ''temperature'' starts to increase while the ''density'' decreases, suggesting that the transition is near saturation. This threshold is consistent with theoretical estimates from laser power

broadening. In the experiment, we maintain the laser power less than the saturation threshold.

D. Optical tagging

Ion spin polarization by optical pumping has been used previously to create test particles in a neutral plasma.[6] Since the mass and charge of spin-polarized ions is the same as other ions, their dynamics is identical, making them ideal test particles.

Figure 10 shows the beam directions and the energy levels of Mg^+ used for test particle transport measurements. Initially, all the ions are in the $S_{1/2}$ state but are unpolarized. To align all the spins, the laser is tuned to the $S_{1/2}$, $m_j = +1/2 \rightarrow P_{3/2}$, $m_j = -1/2$ transition. The lifetime of this excited state is very short (~ 10 ns), and the decay probability to the $S_{1/2}$, $m_j = -1/2$ state is non-negligible, so optical pumping into the $S_{1/2}$, $m_j = -1/2$ state is rapidly achieved. Although velocity-resonant ions in the laser beam path would become polarized at a rate of $(17 \mu s)^{-1}$ for our typical conditions, complete polarization of the thermal spread of axially bouncing ions requires about 50 ms. To tag particles at a particular radius, a second laser is tuned to the $S_{1/2}$, $m_j = -1/2 \rightarrow P_{3/2}$, $m_j = +1/2$ transition, reversing the polarization of these particles. These reversed polarized ions are the test particles.

Detection of test particles is performed with a nondestructive cycling transition. The first laser is tuned to $S_{1/2}$, $m = +1/2 \rightarrow P_{3/2}$, $m = +3/2$, which decays only to $S_{1/2}$, $m_j = 1/2$. Thus, this transition does not change the population of the states that are being probed. However, ''sideband'' excitation of other transitions due to the Lorentzian wings of the
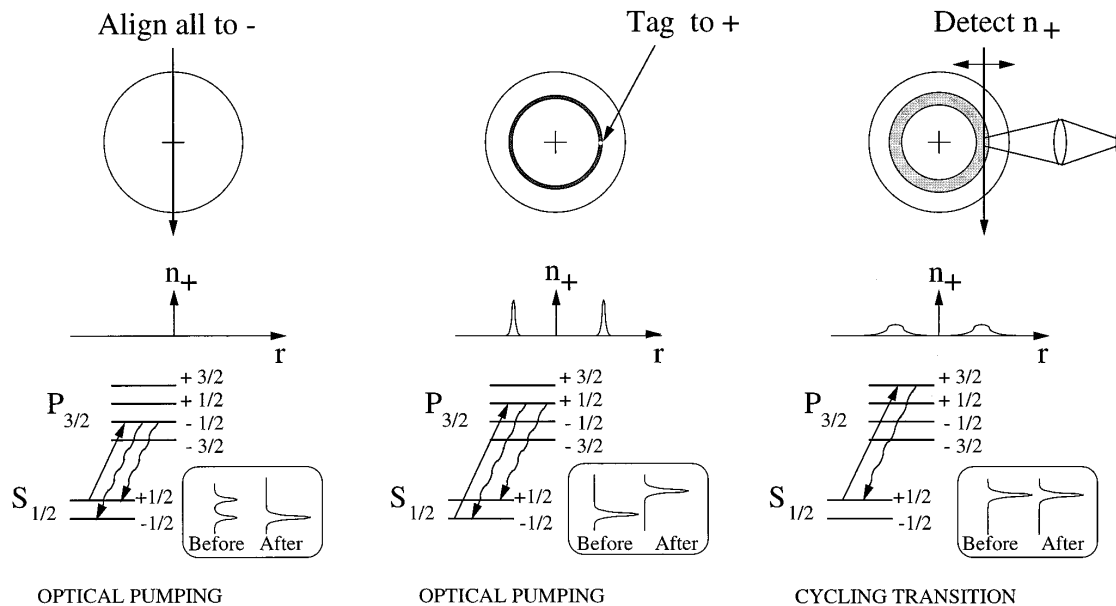

FIG. 10. Schematic representation of the three steps used to measure test particle transport. First, all spins are aligned in the $-1/2$ state, then locally, the test particles are tagged to the $+1/2$ state, and finally the transport of test particles is measured by detecting the population of the $+1/2$ state.
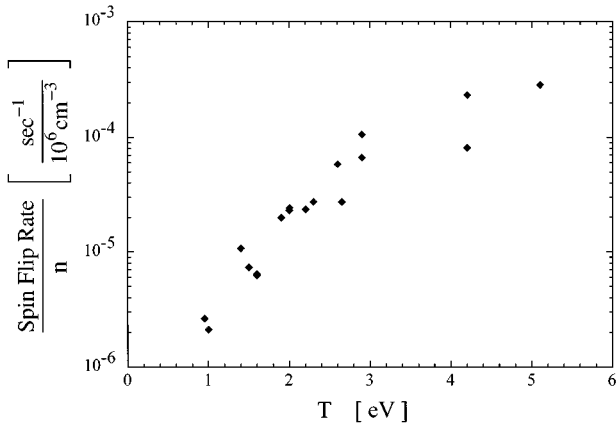
FIG. 11. Measured spontaneous spin flip rate divided by ion density vs ion temperature. For this data, $B=4T$ and the neutral background pressure is $P=7\times10^{-11}$ T.
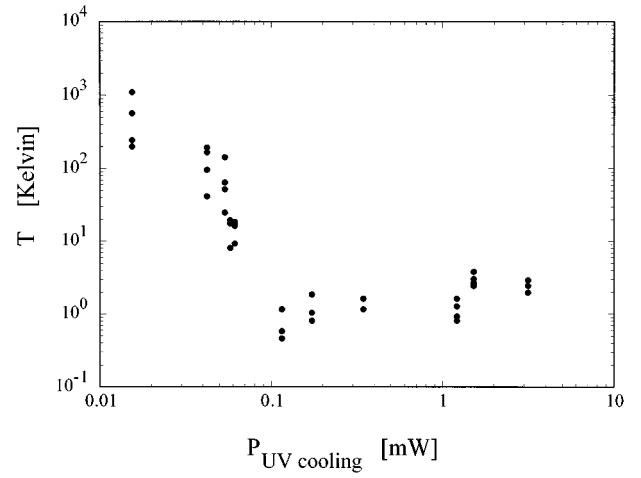

FIG. 12. Preliminary data showing laser cooling vs laser power for a "red-shifted" detuning of 600 MHz: a cloud of 10^9 ions cools to about 1 K for $P_{UV}>0.1$ mW.

laser frequency spectrum will cause weak optical pumping, destroying the polarization of an ion. This effect is crucial for laser cooling experiments,[20] but unwanted in our case. To avoid it, the search beam is weak and is on less than 10% of the time; also, the strong magnetic field helps to minimize sideband pumping.

The tag on an ion can also be lost by spontaneous spin depolarization (i.e., by spontaneous radiative decay or by collisions), but this is much slower than the test particle transport time. The measured spontaneous depolarization rate is a strong function of temperature, as shown in Fig. 11. The spin flip rate is observed to be proportional to ion density n and this dependence has been removed in Fig. 11. Apparently, the spontaneous spin flip is due to ion–ion collisions; but the observed rate is much higher than predicted by theory,[21] and the collision mechanism is not presently understood. Nevertheless, the spin polarization degrades much slower than the time required for the tagged ions to diffuse radially.

E. Plasma manipulation with laser beam

The second laser can also be used to manipulate the plasma temperature by laser cooling or heating. We use the simplest form of laser cooling based on the first-order Doppler effect. A laser beam whose frequency ω_L is slightly lower than the ion resonance frequency ω_0 irradiates the plasma. Ions moving towards the laser beam see the light Doppler shifted toward resonance and, thus, scatter more photons. Hence, more photon momentum is given to an ion moving toward the laser beam than to an ion moving away, and the ion velocity is damped. A comprehensive description of laser cooling can be found in Ref. 18.

Figure 12 shows preliminary results on 10^9 ions laser cooled to a few degrees kelvin with a laser power of 0.1 mW. It is interesting to note that the ion–ion correlation parameter is

$$\Gamma \equiv \frac{e^2}{aT} = \frac{0.58}{T\ \text{(kelvin)}}\left(\frac{n}{10^7\ \text{cm}^{-3}}\right)^{1/3},$$

where a is the mean ion separation defined by $4\pi na^3/3 = 1$. A value of $\Gamma=1$, representing a correlated liquid, appears to be easily reachable in this apparatus.

IV. PLASMA TRANSPORT RESULTS

A. Absolute density calibration

We are able to obtain an absolute calibration of the total charge density from the measurements of the Doppler-shifted resonance peaks; the laser power and light collection efficiencies do not have to be calibrated for this operation. The total rotation of the Mg$^+$ ions is directly obtained from the laser frequency scan data, as

$$\nu_{\text{tot}}(r) \equiv \frac{v_y(x)}{2\pi r} = \frac{f_0(x)-f_0(0)}{f_0(0)}\,c,$$

with f_0 being the frequency of the peak of the distribution function. Here, the detection laser propagates in the $\hat{y}$ direction and is scanned in the $\hat{x}$ direction. The fluorescence is detected from all x at $y=0$, so plasma rotation $v_\theta(r)$ appears as $v_y(x)$. In many cases, the plasma appears to be almost a rigid rotor.[1] To calculate the diamagnetic drift of the Mg$^+$ ions, it is required to differentiate the density and temperature profile. To reduce the experimental noise, smoothing is applied to the profiles; then the diamagnetic drift is calculated as

$$\nu_{\text{dia}}(r) = -\frac{c}{2\pi erBn(r)}\frac{\partial}{\partial r}(nT).$$

The remainder of the rotation frequency is due to $\mathbf{E}\times\mathbf{B}$ drifts in the radial electric field, given by

$$\nu_{\text{tot}}(r) - \nu_{\text{dia}}(r) = \nu_E(r) = \frac{cE_r(r)}{B2\pi r}.$$

The radial electric field E_r arises from the total charge density $n_q(r)$ from Poisson's equation, $(1/r)(\partial/\partial r)(rE_r) = -4\pi en_q$, so the absolute charge density is simply obtained by differentiating ν_E,
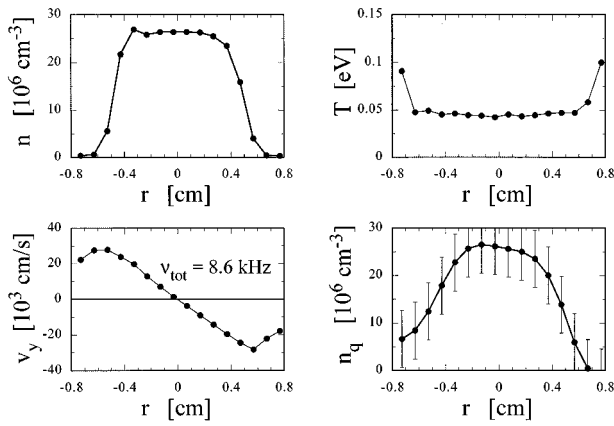
FIG. 13. Measured radial profiles of Mg^+ density n, temperature T, rotation velocity v_y, and calculated total charge density n_q.

$$n_q(r) = -\frac{B}{2ecr}\frac{\partial}{\partial r}\left[r^2 \nu_E(r)\right].$$

Thus, the value of $n_q(r)$ is not dependent on the absolute number of photons received: only the relative gradient $(\partial n/\partial r)n^{-1}$ enters in $\nu_{dia}(r)$, and ν_{dia} is typically small relative to ν_{tot}. Rather, the charge calibration follows from the Doppler frequency shifts, which are very accurately measured when the laser frequency is scanned. Figure 13 represents the three measurements $n(r)$, $T(r)$, and $v_y(r)$ obtained from the fluorescence signal needed to calculate $n_q(r)$.

Noise of the measurement is the intrinsic limitation of the precision of $n_q(r)$ because two derivatives have to be taken in the process. Cold plasmas provide a more accurate determination of the charge profile because the Doppler shift can be measured more accurately.

The ratio of Mg^+ density to total charge density appears to decrease slowly over a period of several days, indicating that Mg^+ ions chemically react with the background neutral gas to form compounds not excited by the laser. Similar slow chemical reactions have been observed in other experiments[22] with Be^9 ions.

B. "Unlimited" ion confinement

Static field errors in a Penning–Malmberg trap exert a drag on confined non-neutral plasmas, causing radial expansion and loss. We have recently developed a "rotating wall" technique whereby this transport can be counteracted by applying an electrostatic wall asymmetry rotating faster than the plasma.[7] This causes inward radial transport and plasma compression,[7] resulting in a steady-state balance. Ions are routinely confined for more than two weeks without any change in the density. The confinement time is limited by the liquid-helium holding capacity of the superconducting coil. The rotating wall asymmetry also heats the plasma; the ion temperature reaches an equilibrium, which is controlled by the amplitude of the rotating wall signal and the collisions with the neutrals, which provide the cooling. We note that the rotating wall technique also works with pure electron plasmas if sufficient cooling is provided by cyclotron radiation or other means.

Figure 13 shows that the plasma has relaxed to a stable equilibrium, rotating like a rigid rotor, with constant temperature inside the plasma. These conditions indicate that the ion cloud has relaxed to a near global thermal equilibrium.[1] We should underline that this is a unique property of non-neutral plasmas, namely that they can relax to thermodynamic equilibrium and still remain confined.

C. Test particle transport

Transport of test particles across the magnetic field in a plasma close to thermal equilibrium is an important subject in non-neutral plasma physics. The theoretical literature presents various models for test particle transport. We have performed detailed measurements of test particle transport[23] with the present apparatus.

The basic scheme used to measure radial test particle transport is shown in Fig. 10. The first step is to optically pump the entire plasma into one spin state with a perpendicular beam passing through the center. The beam is left on long enough to ensure that all ions have had a chance to pass through the beam due to their $\mathbf{E}\times\mathbf{B}$ rotation and bounce motion, so 100% of optical pumping is obtained. Then a "tag" beam parallel to the magnetic field reverses the spin orientation, creating the test particles at position r_t. The tag beam is left on long enough to label a hollow tube defined by the $\mathbf{E}\times\mathbf{B}$ rotation of the plasma through the tag beam. The transport of test particles is then measured by a search beam tuned to a cycling transition. At each radial location r_s of the search beam, the density of test particles is recorded as a time series $n_t(r_s,t)$. Then the full profile of test particles $n_t(r,t)$ is obtained by successive repetition of the three previous steps for different search radii.

Fluxes of test particles $\Gamma_t(r,t)$ are calculated from measured quantities as

$$\Gamma_t(r,t) = -\frac{1}{r}\int_0^r dr' r' \frac{\partial}{\partial t} n_t(r',t)$$
$$+ \int_0^r dr' r' \frac{2n_t(r',t) - n(r')}{\tau_s(r')}.$$

The second term has been added to account for the small but nonzero source term due to spontaneous spin flip. The spontaneous spin flip time τ_s is experimentally measured. With this correction, the total number of test particles is conserved to within 10% over the entire 30 s measurement.

The measured fluxes are compared with a model of transport taking into account diffusion with coefficient $D_{ii}(r)$, and mobility with velocity $V_m(r)$,

$$\Gamma_t(r,t) \equiv D_{ii}(r)n(r)\frac{\partial}{\partial r}\frac{n_t(r,t)}{n(r)} + V_m(r)n_t(r,t).$$

The measured normalized flux is plotted versus the measured normalized gradient in Fig. 14; the different points correspond to different times after the localized tagging. The straight line on the data justifies the validity of the diffusion model. Also, the mobility term is found to be very small
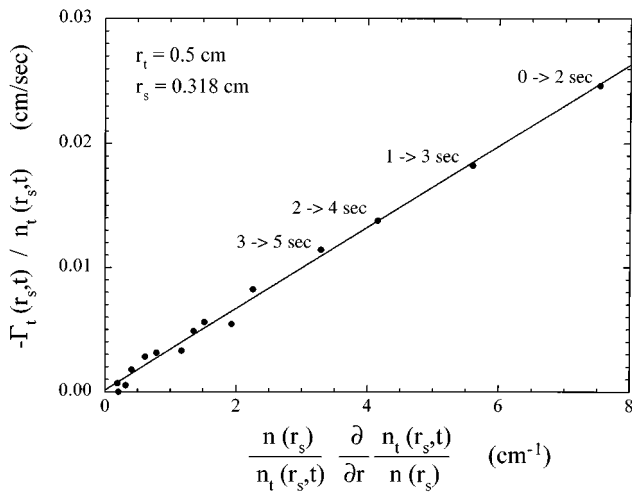
FIG. 14. Measured normalized test particle flux Γ_t/n_t vs normalized test particle gradient $(n/n_t)(\partial/\partial r)(n_t/n)$, showing Fick's law of diffusion. The slope of the fitted line is the diffusion coefficient.

compared to the diffusion term, as it must be for a steady-state plasma. The slope of the line is the diffusion coefficient at the search radius r_s.

The measured diffusion coefficients appear to be faster than the predicted one produced by classical Boltzmann theory by a factor of about 10. Detailed data on the scaling of the diffusion with density, temperature, and magnetic field can be found in Ref. 23. This enhanced diffusion rate is consistent with enhanced bulk viscosity previously measured in electron plasmas, and is probably due to long-range ''$\mathbf{E} \times \mathbf{B}$ drift collisions'' between the ions. These long-range collisions should also give rise to enhanced heat transport. Both the bulk viscosity and the heat conductivity should be measurable with this apparatus, so we are confident that it will continue to be scientifically productive.

ACKNOWLEDGMENTS

[1] C. F. Driscoll, J. H. Malmberg, and K. S. Fine, Phys. Rev. Lett. **60**, 1290 (1988); L. R. Brewer, J. D. Prestage, J. J. Bolllinger, W. M. Itano, D. I. Larson, and D. J. Wineland, Phys. Rev. A **38**, 859 (1988).
[2] J. H. Malmberg and C. F. Driscoll, Phys. Rev. Lett. **44**, 654 (1980).
[3] C. F. Driscoll and J. H. Malmberg, Phys. Rev. Lett. **50**, 167 (1983); C. F. Driscoll, K. S. Fine, and J. H. Malmberg, Phys. Fluids **29**, 2015 (1986); J. Notte and J. Fajans, Phys. Plasmas **1**, 1123 (1994).
[4] S. M. Crooks and T. M. O'Neil, Phys. Plasmas **2**, 355 (1995); B. P. Cluggish and C. F. Driscoll, Phys. Rev. Lett. **74**, 4313 (1995).
[5] D. L. Eggleston, T. M. O'Neil, and J. H. Malmberg, Phys. Rev. Lett. **53**, 982 (1984).
[6] F. Skiff, F. Anderegg, T. Good, and P. J. Paris, Phys. Lett. A **137**, 57 (1989).
[7] X.-P. Huang, F. Anderegg, E. M. Hollmann, C. F. Driscoll, and T. M. O'Neil, Phys. Rev. Lett. **78**, 875 (1997).
[8] C. F. Driscoll, in *Low Energy Antimatter*, Vol. 184, edited by David Cline (World Scientific, Singapore, 1986).
[9] R. A. McGill, I. G. Brown, and J. E. Galvin, Rev. Sci. Instrum. **61**, 580 (1990).
[10] E. Sarid, F. Anderegg, and C. F. Driscoll, Phys. Plasmas **2**, 2895 (1995).
[11] K. S. Fine, Ph.D. thesis, UCSD (1988).
[12] D. L. Eggleston, C. F. Driscoll, B. R. Beck, A. W. Hyatt, and J. H. Malmberg, Phys. Fluids B **4**, 3432 (1992).
[13] D. J. Larson, J. C. Bergquist, J. J. Bollinger, W. M. Itano, and D. J. Wineland, Phys. Rev. Lett. **57**, 70 (1986).
[14] D. N. Hill, S. Fornaca, and M. G. Wickman, Rev. Sci. Instrum. **54**, 309 (1983).
[15] R. Koslover and R. McWilliams, Rev. Sci. Instrum. **57**, 2441 (1986).
[16] J. C. Bergquist, H. Hemmati, and W. M. Itano, Opt. Commun. **43**, 437 (1982).
[17] R. E. Drullinger, D. J. Wineland, and J. C. Bergquist, Appl. Phys. **22**, 365 (1980).
[18] D. J. Wineland and W. M. Itano, Phys. Rev. A **20**, 1521 (1979).
[19] J. T. Davies and J. M. Vaughan, Astrophys. J. **137**, 1302 (1963); J. T. Twitty, P. L. Rarig, and R. E. Thompson, J. Quant. Spectrosc. Radiat. Transfer **24**, 529 (1980).
[20] D. J. Wineland, J. C. Bergquist, W. M. Itano, and R. E. Drullinger, Opt. Lett. **5**, 245 (1980).
[21] D. Z. Jin and D. H. E. Dubin (private communication). Similar calculations of Coulomb excitation can be found in K. Alder, A. Bohr, T. Haas, B. Mottelson, and A. Winther, Rev. Mod. Phys. **28**, 432 (1956).
[22] J. J. Bollinger (private communication). See also, D. J. Wineland, J. C. Bergquist, J. J. Bollinger, W. M. Itano, D. J. Heizen, S. L. Gilbert, C. H. Manney, and M. G. Raizen, IEEE Trans. Ultrason. Ferroelectr. Freq. Control **37**, 515 (1990).
[23] F. Anderegg, X.-P. Huang, C. F. Driscoll, E. M. Hollmann, T. M. O'Neil, and D. H. E. Dubin, Phys. Rev. Lett. **78**, 2128 (1997); F. Anderegg, X.-P. Huang, E. M. Hollmann, C. F. Driscoll, T. M. O'Neil, and D. H. E. Dubin, Phys. Plasmas **4**, 1552 (1997).